Sustainable ironmaking from low-grade iron ores: A kinetic study on thermal decomposition and reduction of iron (II) oxalate

Antonio Trinca [a,*], Nicola Verdone [a], Özge Özgün [c], Yan Ma [b,c] (ORCID), Isnaldi R. Souza Filho [d], Dierk Raabe [c], Giorgio Vilardi [a]

[a] *"Sapienza" University of Rome, Dept. of Chemical Engineering Materials Environment, via Eudossiana 18, Rome 00184, Italy*
[b] *Department of Materials Science and Engineering, Delft University of Technology, Mekelweg 2, Delft 2628 CD, the Netherlands*
[c] *Max Planck Institute for Sustainable Materials, Max-Planck-Straße 1, Düsseldorf 40237, Germany*
[d] *Institut Jean Lamour, CNRS (UMR 7198), Université de Lorraine, Nancy F-54000, France*

ARTICLE INFO

ABSTRACT

Decarbonization solutions enabling the use of low-grade iron ores are essential for a sustainable steel industry, reducing dependence on scarce high-grade ores and environmental impact. Current processes mainly require high-grade ores, highlighting the need for efficient methods to process lower-quality feedstocks. This study explores a hydro-pyrometallurgical approach for sustainable production. Dihydrate ferrous oxalate, obtained via oxalic acid extraction of iron oxide, was analyzed by thermogravimetric analysis (TGA) and differential scanning calorimetry (DSC), with postmortem samples characterized by X-ray powder diffraction. Non-isothermal experiments were conducted from 25 to 800 °C at 2, 5, and 10 °C/min under inert (argon) and reducing (carbon monoxide and hydrogen) atmospheres. The curves show three main steps: dehydration, decomposition, and, under reducing conditions, reduction to metallic iron. In carbon monoxide, iron carbide formation and graphitic carbon deposition were also observed. DSC revealed endothermic peaks for dehydration and decomposition and in carbon monoxide, a strong exothermic peak, due to the reverse Boudouard reaction. Activation energies were calculated using the Kissinger method. Dehydration showed an activation energy of 62 kJ/mol in argon and carbon monoxide, and slightly lower in hydrogen (58 kJ/mol), likely due to faster diffusion. Decomposition appeared gas independent, with an activation energy of 90 kJ/mol. A mathematical model was developed to relate reaction conversion to time at a fixed heating rate. The model accurately fits the experimental data and remains valid even at higher heating rates, comparable to industrial conditions. This kinetic model supports simulation and scale-up of the iron oxalate reduction process.

1. Introduction

The steel industry is facing critical challenges that will shape its future as well as the future of human society. Steel is, in terms of mass, with its 1.8 billion tons produced each year [1], the second most widely used material by humanity, after concrete. Its demand is expected to grow in the coming years, with projections indicating an increase of up to 11 % by 2030 compared to 2020, highlighting the ongoing upward trend in global steel consumption driven by infrastructure, construction, industry, mobility and the energy sector [2,3]. Primary growth in this and the next decades will take place due to the massively growing industrialization in developing nations, particularly in countries like India, Indonesia and various regions across Africa. However, the steel industry is one of the largest contributors to greenhouse gas emissions, accounting for ~ 8 % global emissions [4–6]. A promising solution to producing green steel while reducing carbon dioxide (CO_2) emissions is the direct reduction process using green hydrogen (HyDR) [5,7–9]. In this process, water is the only by-product from the redox reaction, allowing iron to be produced without CO_2 emissions. HyDR processes face limitations including high energy consumption for hydrogen production and dependency on the availability of renewable energy. Additionally, maintaining high-temperature conditions and controlling the process efficiently can be challenging at industrial scale. Furthermore, the reliance on high-grade iron ore (Fe > 65 %) for direct reduced iron (DRI) production presents significant challenges related to resource availability. High-grade ores are limited and unevenly distributed globally, leading to supply constraints and price volatility. This

---

Nomenclature

Ar	Argon	Fe_3C	Cementite
β	Heating Rate	h	Hour
C	Carbon	HCl	Hydrochloric acid
°C	Celsius degree	HyDR	Hydrogen Direct Reduced Iron
CO	Carbon Monoxide	H_2	Hydrogen
CO_2	Carbon Dioxide	H_2O	Water
DRI	Direct Reduced Iron	H_2SO_4	Sulfuric acid
DSC	Differential Scanning Calorimetry	g	Gram
E_a	Activation Energy	J	Joule
EAF	Electric Arc Furnace	k_D	Gaseous Diffusion Rate Constant
$Fe_2(C_2O_4)_3$	Ferric Oxalate	l	Liter
FeC_2O_4	Ferrous Oxalate	M	Molarity
$FeC_2O_4 \cdot 2H_2O$	Dihydrate Ferrous Oxalate	min	Minute
Fe	Iron	s	Second
FeO	Wüstite	T	Temperature
Fe_2O_3	Hematite	t	Time
Fe_3O_4	Magnetite	TGA	Thermogravimetric analysis
		X	Conversion
		XRD	X-ray Powder Diffraction

dependence not only increases production costs but also limits the flexibility of the steel industry to respond to fluctuations in raw material supply. Therefore, reducing reliance on these high-quality ores is critical for both economic and environmental sustainability. As a result, developing sustainable methods to produce steel from low-grade iron ore and waste streams has gained significant attention [10–12].

A viable alternative to conventional primary steel production methods is the hydrometallurgical route. Several studies have analysed the selective dissolution of iron oxides from low-grade iron ores using oxalic acid [13–15]. The dissolution process has recently gained attention as a crucial reaction in the development of clean iron production methods [16].

The dissolution of iron oxides (hematite, magnetite, goethite) can be achieved using inorganic or organic acids. Inorganic acids (e.g., H_2SO_4, HCl) risk contaminating the product and the environment, whereas organic acids, particularly oxalic acid, offer selective iron leaching with minimal contamination because they form stable iron.

The mechanism of oxalic acid dissolution involves three steps: (1) adsorption of ligands on the iron oxide surface, creating active sites; (2) nonreductive dissolution, enhanced by low pH and high temperature; and (3) reductive dissolution, where Fe^{2+} formation accelerates iron removal through an autocatalytic process. Magnetite, containing Fe^{2+}, dissolves faster, while hematite requires slower Fe^{2+} generation via electron transfer from the ligand.

Key factors affecting dissolution rate include pH, oxalic acid concentration, and temperature. The solution is most effective around pH 2.5–3.0, though practical limitations often require buffering with alkali salts. Higher temperatures (> 80–90 °C) and higher acid concentrations increase dissolution rates.

Oxalic acid is particularly selective for iron, avoiding contamination from other metals, and is effective in both nonreductive and reductive dissolution. For industrial processes, dissolution must occur in the dark using only iron oxides and oxalic acid, as light or other additives can reduce selectivity or produce low-quality Fe (II) oxalate. Productivity thus depends mainly on the concentrations of oxalic acid and iron oxide, as well as temperature, under strongly acidic conditions to prevent Fe^{2+} reoxidation.
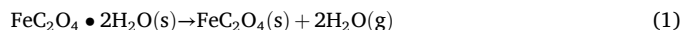
Santawaja et al. [17] investigated three low-grade iron sources (IO-A, IO-B, and CS), treated through dissolution in oxalic acid followed by photochemical reduction. Dissolution with 1 M $H_2C_2O_4$ led to a key result: a significant increase in iron purity, which rose from 33.9 % to 93.3 % in the raw materials to values above 80 %, reaching 99.7 % for IO-A.

This step allows for the production of an aqueous solution of iron (III) salts, while the undissolved metals can be easily separated from the solution. The resulting solution exhibits interesting properties under light exposure. Due to its photosensitivity, the iron (III) salt is reduced to iron (II), specifically upon excitation within the tropospheric solar UV–visible region (approximately 290–570 nm) [18,19]. During photochemical reduction, the precipitation of iron (II) oxalate dihydrate crystals, with a very low solubility in water (approximately 22 mg/L), occurs [19].
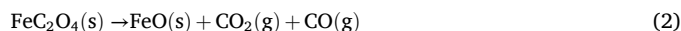
Tanvar et al. [20] developed a process to produce iron oxalate from red mud. The method begins with an acid washing step using HCl to remove calcium and sodium. The resulting solid is then subjected to leaching with oxalic acid, yielding a solution rich in iron oxalate. By exploiting the photosensitivity of this solution, it was possible to obtain ferrous oxalate with a purity greater than 99 %.

Based on these phenomena, Santawaja et al. [17] proposed an intriguing process for the potential production of sustainable iron from low grade iron ores. The process consists of three steps: an initial dissolution step, followed by a photoreduction step that forms iron (II) oxalate, and a final pyroreduction step, where the metal salt is reduced to metallic iron using gaseous hydrogen (H_2). As highlighted in the work of Hickling [21], the pyroreduction process of iron (II) oxalate occurs in three stages: dehydration, decomposition into iron oxides, and reduction to metallic iron. This reaction sequence takes place according to the reactions (1)–(9).
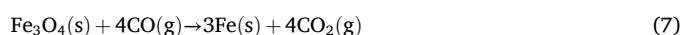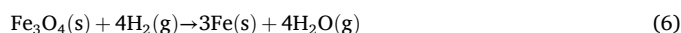
Dehydration:

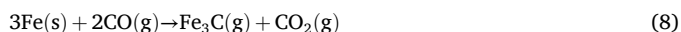$$FeC_2O_4 \bullet 2H_2O(s) \rightarrow FeC_2O_4(s) + 2H_2O(g) \tag{1}$$

Decomposition:

$$FeC_2O_4(s) \rightarrow FeO(s) + CO_2(g) + CO(g) \tag{2}$$

Disproportionation:

$$4FeO(s) \rightarrow Fe(s) + Fe_3O_4(s) \tag{3}$$

Solid-gas reduction:

$$FeO(s) + H_2(g) \rightarrow Fe(s) + H_2O(g) \tag{4}$$

$$FeO(s) + CO(g) \rightarrow Fe(s) + CO_2(g) \tag{5}$$

$$Fe_3O_4(s) + 4H_2(g) \rightarrow 3Fe(s) + 4H_2O(g) \tag{6}$$

$$Fe_3O_4(s) + 4CO(g) \rightarrow 3Fe(s) + 4CO_2(g) \tag{7}$$

Carburization:

$$3Fe(s) + 2CO(g) \rightarrow Fe_3C(g) + CO_2(g) \qquad (8)$$

Boudouard reaction:

$$C(s) + CO_2(g) \rightleftharpoons 2CO(g) \qquad (9)$$

Prior to the reduction reactions, iron oxalate transitions from its dihydrate form ($FeC_2O_4 \cdot 2H_2O$) to the anhydrous phase (FeC_2O_4) through a dehydration reaction occur (1). As the temperature increases, iron (II) oxalate starts to decompose into wüstite (FeO), releasing CO (carbon monoxide) and CO_2 (2). At temperatures below 570°C, wüstite disproportionates into iron (Fe) and magnetite (Fe_3O_4) (3). Finally, both wüstite and magnetite can be reduced to metallic iron in the presence of reducing agents, such as gaseous H_2 or CO (4)–(7). In the presence of CO gas, the reactions involve carbon deposition and the carburization of iron (8, 9).

Recently, Trinca et al. [22] evaluated a hydro-pyrometallurgical process that begins with the dissolution of low-grade ores using oxalic acid, followed by reduction to metallic iron and its conversion into steel. An assessment of the process examined its technical feasibility as well as its economic viability. The study emphasized the advantages of producing green steel via the oxalate-based process with a lower H_2 consumption compared with other green steel production methods, despite high energy costs of the process. Specifically, the study proposed reusing the CO generated during the decomposition reaction (2) as a reducing agent for the reduction of iron oxides, which are also formed during the decomposition. In the proposed route, oxalic acid is regenerated by the electrolytic reduction of CO_2, which requires an external CO_2 source, while hydrogen is obtained through alkaline water electrolysis. According to the results, it is possible to produce green steel at a levelized cost of 1093.32 $/$t_{STEEL}$, assuming renewable electricity cost of 30 $/MWh. The main challenge of the process is its substantial energy requirement, which mainly stems from the electricity demand of the electrolyzers. However, as electrolyzer efficiency improves in the future, a reduction in energy consumption is expected, which would also drive down production costs.

The behaviour of iron (II) salts under various atmospheres is a topic widely discussed in the literature [23–26]. Using thermogravimetric analysis (TGA), a study was conducted on the thermally induced solid-state transformations of $FeC_2O_4 \cdot 2H_2O$ in a closed environment [24]. The solid sample is encapsulated and isolated inside an aluminium capsule, then heated to temperatures up to 640 °C at a rate of 5 °C/min. In this way, the formation of all possible gaseous products (CO, CO_2, H_2O) in the reaction system is enabled, leading to the decomposition of the oxalate into a solid composed of wüstite and iron. In contrast, Hermankova et al. [23], investigated the thermal decomposition of ferric oxalate tetrahydrate, $Fe_2(C_2O_4)_3 \cdot 4H_2O$, in inert and oxidative atmospheres. In both cases, the intermediate formation of FeC_2O_4 was found during the decomposition of $Fe_2(C_2O_4)_3$. Subsequently, the ferrous oxalate decomposes into wüstite in an inert atmosphere, while in an oxidative atmosphere, the oxalate decomposed and simultaneously the iron oxidized, resulting in a final solid composed of hematite (Fe_2O_3). Carles et al. [25] investigated the thermal decomposition of $FeC_2O_4 \cdot 2H_2O$ under Ar (argon), H_2/Ar mixture, and H_2, with a heating rate of 2 °C/min, resulting in a mixture of FeO, Fe, CO, and CO_2. All these studies implemented non-isothermal tests with low heating rates (2–10 °C/min). This is because the three reaction steps (dehydration, thermal decomposition, and reduction) occur simultaneously at high temperatures. At high heating rates (> 50 °C/min), these steps would not be distinguishable, preventing a proper kinetic analysis of the competing phenomena.

Another study [26] investigated the thermal dehydration of α- and β-phase ferrous oxalate dihydrate particles with distinct shapes. A combined kinetic model, covering induction period, surface reaction, and phase boundary reaction, was developed to explain the observed sigmoidal mass-loss behaviour.

The model accurately simulated the dehydration kinetics under various conditions, including inert and oxidative atmospheres, non-isothermal conditions at a single heating rate of 10 °C/min, and isothermal conditions in the range of 121–145 °C.

A comprehensive kinetic model for the three reaction steps is essential for advancing process design and optimization in hydro-pyrometallurgical steel production from low-grade iron ores. Understanding the behaviour of iron (II) oxalate under CO flow is fundamental, as CO-based reduction offers significant process advantages, including iron carburization and energy savings due to the exothermic nature [22]. Thus, it is crucial to develop kinetic models for the dehydration and reduction steps. This study aims to identify the kinetic mechanisms for the behaviour of iron (II) oxalate in inert and reducing environments. To achieve this, the reaction kinetics was investigated using TGA during non-isothermal tests at different heating rates. The post-mortem samples were analysed using X-ray Powder Diffraction (XRD) to determine their final composition.

2. Experimental

2.1. Materials

Iron (II) oxalate dihydrate powder was purchased from the Thermo Scientific Chemicals platform. It has a purity of over 99 %. The original sample was characterized by XRD. The powder has a mean particle diameter of 20 μm.

2.2. Thermal analyses of oxalate decomposition and reduction

The TGA measurements were conducted using the SETARAM TG 96 system. The setup consisted of a vertical alumina tube reactor built around a balance with high accuracy (10^{-6} mg). The weights of the initial samples for each test ranged between 275 and 285 mg. The oxalate samples were placed in an alumina crucible, which was suspended by a Nichrome wire connected to the balance beam. The tubular furnace, controlled by a temperature programmer, enabled a linear increase in the sample temperature. The reactor was heated using electrical graphite heating elements. Precise temperature control was ensured by a S-type (Pt/Pt-Rh) thermocouple positioned very close to the sample crucible. Once the sample was placed in the balance, a primary vacuum was created using a vane pump to eliminate air present in the interior of the furnace, then it was filled with the desired gas up to atmospheric pressure. Gas flows were regulated by Bronkhorst mass flow controllers. The sample was placed under a constant gas flow of 10 l/h of high-purity H_2, CO, or Ar (99.999 %). The tests were conducted by replicating the same conditions (temperature, gas composition, and flow rate) using an empty crucible (blank test). The TGA curve obtained from the blank test was subtracted from the curve of the actual test in order to suppress the effects of the crucible's thermal expansion due to the temperature. All tests were conducted under non-isothermal conditions, with a heating rate (β) of 2, 5, or 10 °C/min, heating from a temperature of 20 up to 800 °C. The samples were then held at 800 °C for 5 min and finally cooled in Ar at a cooling rate of 10 °C/min. In experiments conducted at a heating rate of 5 °C/min, the TGA tests were coupled with Differential Scanning Calorimetry (DSC), using a Discovery SDT 650 TA instrument.

Solid decomposition products were identified by X-ray diffraction (XRD) using a RIKAKU SMARTLAB 9KW diffractometer with Cu $K_{\alpha1}$ radiation ($\lambda = 1.54059$ Å). The scanning range 2θ ranged from 10° to 100° with a scanning step of 0.01° and a scanning speed of 2° min^{-1}.

2.3. Kinetic modelling

Several authors employed the Kissinger method as one of the established fitting approaches that can be applied to analyse a series of experiments with varying linear heating rates [27]. Its strength lies in requiring only the temperature at which the maximum reaction rate
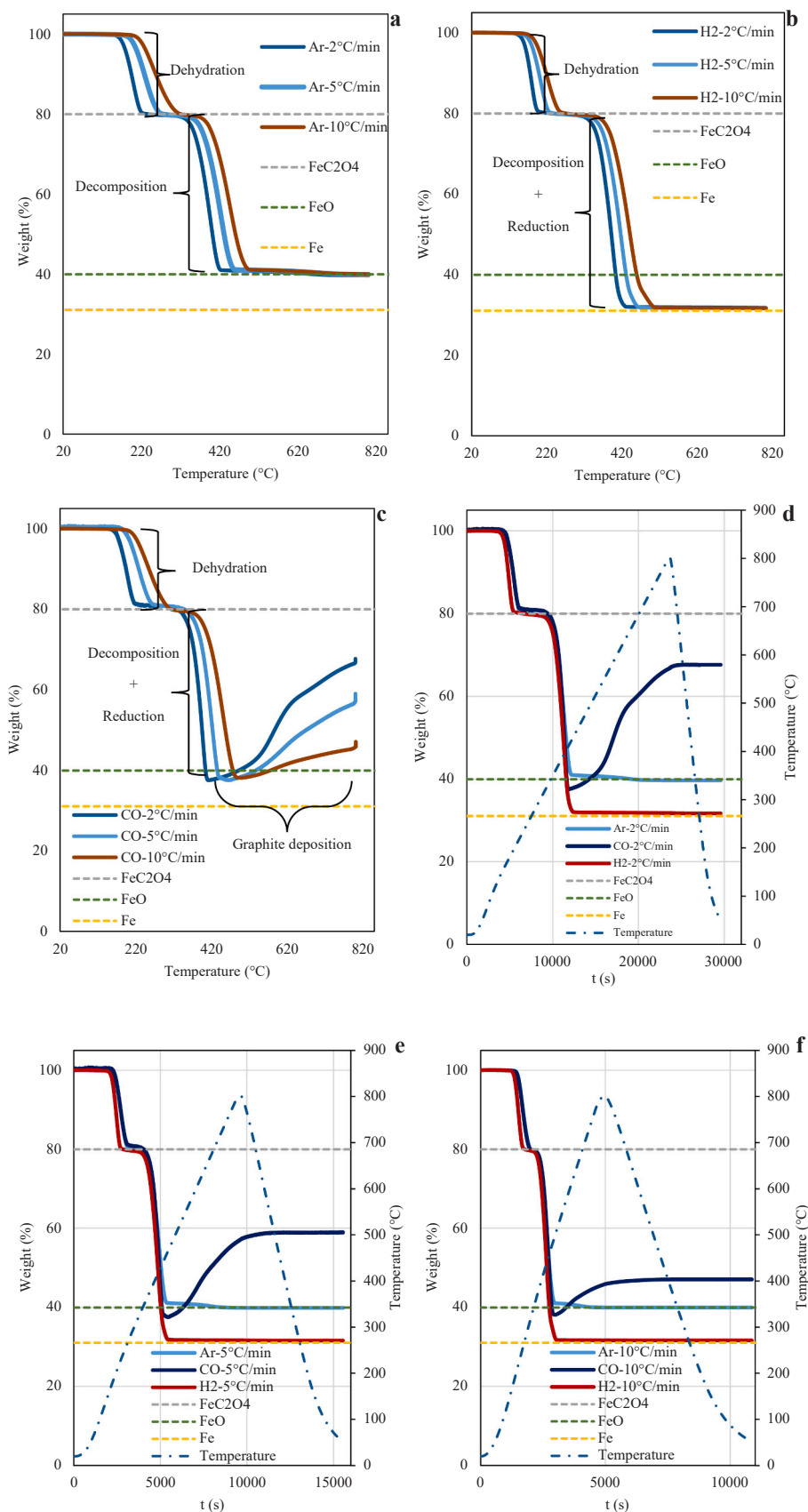
Fig. 1. The weight changes of the samples in 1a Ar, 1b H$_2$, and 1c CO atmospheres as a function of temperature; and at different heating rates of 1d 2 °C/min, 1e 5 °C/min, 1f 10 °C/min as a function of time.

Table 1
Times, temperatures, and peak temperatures of the dehydration, decomposition, and reduction steps derived from thermogravimetric curves, and determination of the activation energy through the Kissinger relation (Eq. (10)).

β (°C/min)		2	5	10
Dehydration				
Ar	t_{in}-t_{fin} (s)	4014–6682	2100–3219	1375–2024
	T_{in}-T_{fin} (°C)	147–238	166–276	191–322
	T_m (°C)	199	229	253
	E_a (kJ/mol)	**62.19**		
CO	t_{in}-t_{fin} (s)	4290–6801	2112–3512	1342–2001
	T_{in}-T_{fin} (°C)	146–242	167–302	191–317
	T_m (°C)	196	232	253
	E_a (kJ/mol)	**62.15**		
H₂	t_{in}-t_{fin} (s)	3660–6550	1903–2855	1223–1774
	T_{in}-T_{fin} (°C)	134–233	142–241	160–273
	T_m (°C)	179	202	221
	E_a (kJ/mol)	**58.55**		
Decomposition				
Ar	t_{in}-t_{fin} (s)	6684–18,194	3219–8138	2024–4432
	T_{in}-T_{fin} (°C)	238–623	276–690	322–744
	T_m (°C)	396	423	447
	E_a (kJ/mol)	**90.29**		
CO	t_{in}-t_{fin} (s)	6801–11,642	3512–5087	2001–2855
	T_{in}-T_{fin} (°C)	242–404	302–435	317–476
	T_m (°C)	396	421	451
	E_a (kJ/mol)	**89.51**		
H₂	t_{in}-t_{fin} (s)	6560–11,582	2855–5023	1774–2749
	T_{in}-T_{fin} (°C)	233–402	241–429	273–458
	T_m (°C)	393	417	438
	E_a (kJ/mol)	**90.45**		
Reduction				
CO	t_{in}-t_{fin} (s)	11,642-	5087-	2855-
	T_{in}-T_{fin}	404-	435-	476-
	T_m (°C)	404	436	477
	E_a (kJ/mol)	**92.75**		
H₂	t_{in}-t_{fin} (s)	11,582–12,970	5023–9773	2749–3004
	T_{in}-T_{fin} (°C)	402–448	429–469	458–503
	T_m (°C)	402	429	458
	E_a (kJ/mol)	**91.52**		

occurs for different linear heating rates as input parameter, without requiring deeper knowledge about the underlying reaction mechanism. The method is based on the Arrhenius equation and assumes that the process follows a first-order reaction model or that the reaction rate exhibits a single dominant maximum. This relationship allows the evaluation of the activation energy from thermal analysis data. By incorporating the heating rate (β), the Kissinger Eq. (10) is derived [28] as

$$\ln\left(\frac{\beta}{T_m^2}\right) = \frac{-E_a}{RT_m} + \ln\left(\frac{AR}{E_a}\right) + \text{constant} \tag{10}$$

where A is the preexponential factor, R (J mol^{-1} K^{-1}) is the constant gas, E_a (J mol^{-1}) the activation energy, T_m (K) is the temperature at which the maximum reaction rate is reached for a given heating rate. Thus, conducting a series of experiments with different linear heating rates should result in a straight line when the left-hand side of Eq. (10) is plotted against $1/T_m$. The slope of this line provides the activation energy.

An additional mathematical fitting of the experimental curves was performed. This allowed deriving a relationship to determine the reaction rate as a function of the considered heating rate.
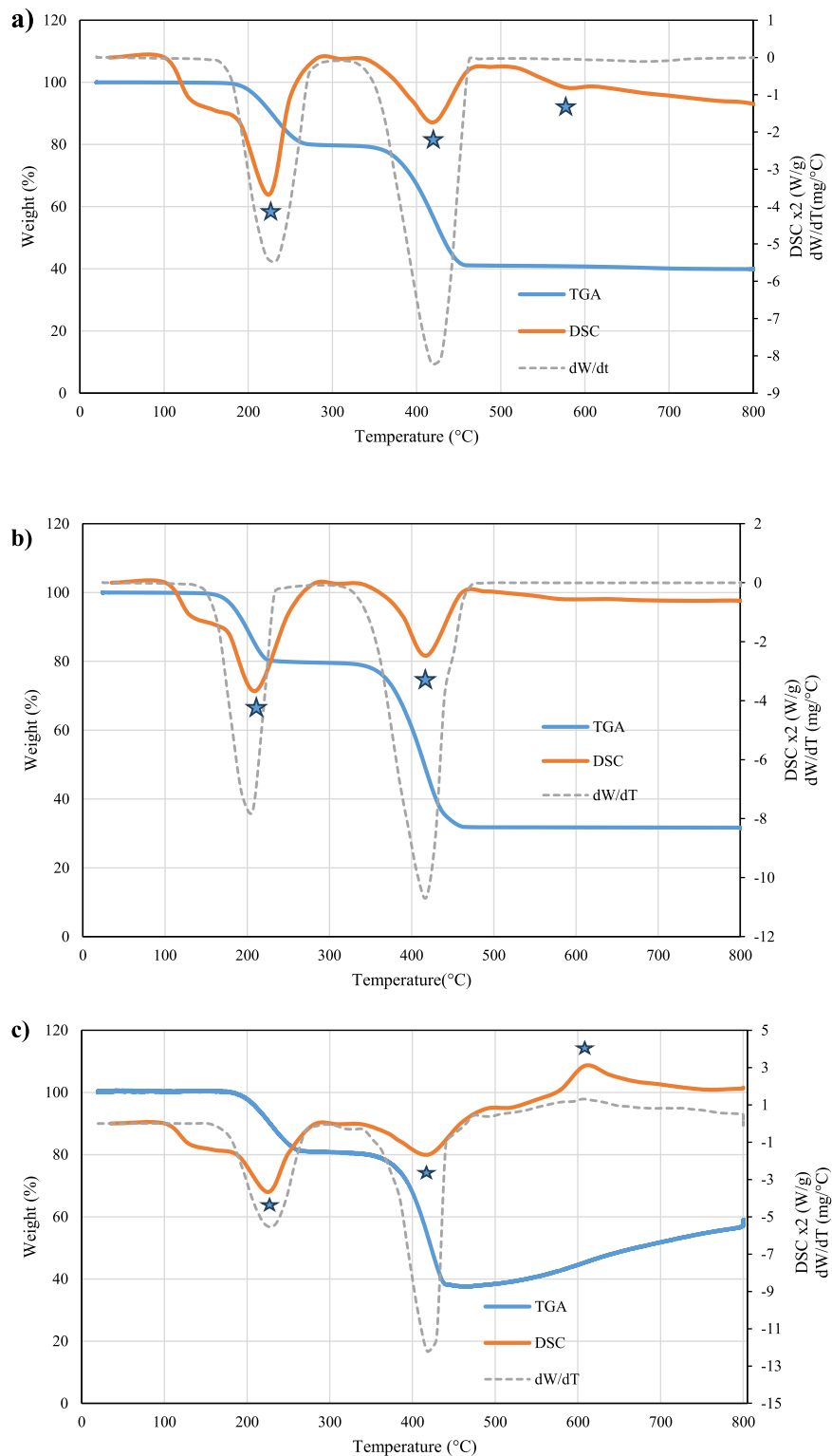
3. Results

The TGA curves for samples tested in three gases (Ar, CO, and H₂) are shown in Fig. 1. The graphs reveal the weight loss in percentage as a function of temperature (a, b, c) and time (d, e, f). The trend of the curves is similar in all cases showing a continuous weight loss, except for the CO case with a weight gain in the end of reaction. A first dehydration
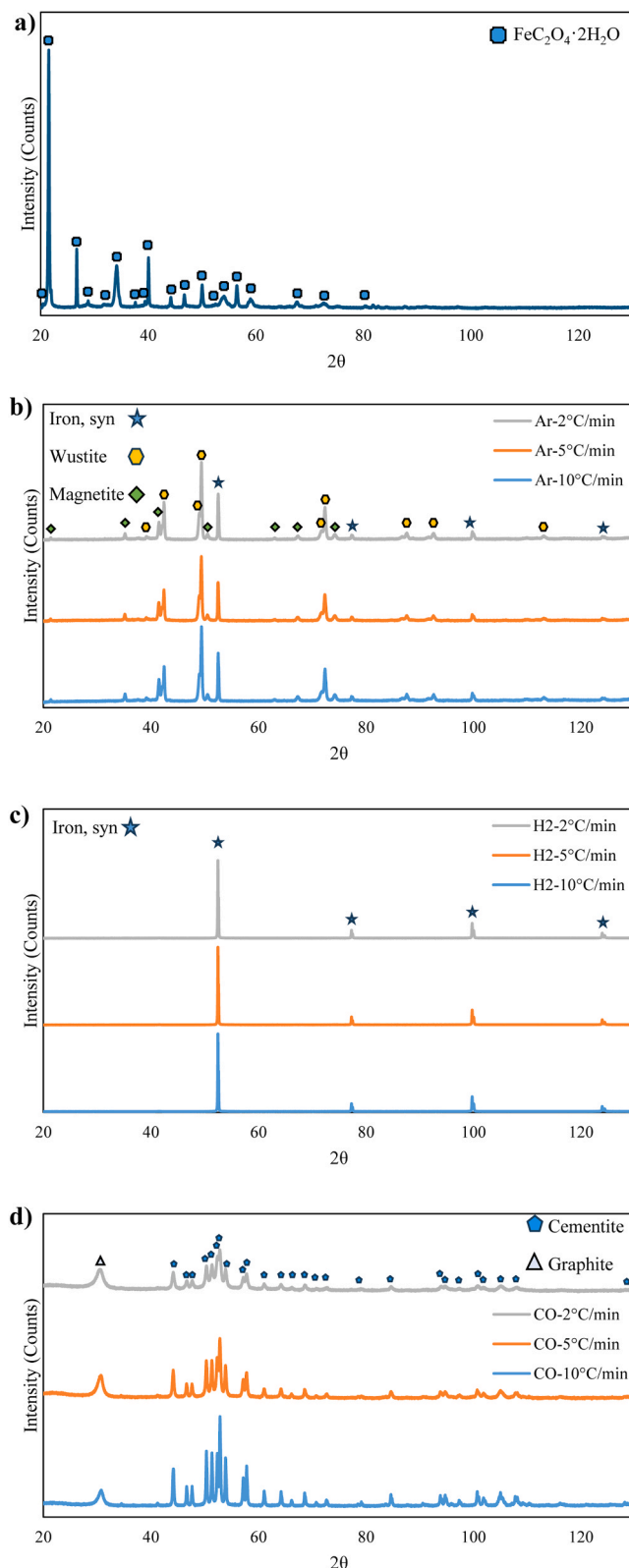
Fig. 2. X-ray Powder Diffraction analysis: 2a initial sample; samples after testing in 2b Ar, 2c H₂, and 2d CO.

step is observed in a lower temperature range (Table 1). The weight curve reaches a plateau around 79.9 %, indicating that all the water (20.1 % of the theoretical initial weight) has evaporated (Fig. 1a). As the temperature increases, the decomposition of iron (II) oxalate begins. For Ar, the decomposition reaction results in a further weight loss of 39.9 %,

Fig. 3. Differential scanning calorimetry (DSC) and thermogravimetric analysis (TGA) with the derivative of the TGA curve with respect to temperature (dW/dT) results for the samples heated up at a heating rate of 5 °C/min in 3a Ar, 3b H_2, and 3c CO atmospheres.

matching the expected value for wüstite, which is approximately 39.9 % of the initial mass. Then, the TGA curve halts and no further weight change is observed with a further increase in the temperature to 800 ℃. In contrast, the TGA curves of the samples in CO (Figure 1c) and H_2 (Fig. 1b) atmospheres continue declining due to the reduction of wüstite to metallic iron.

Under H_2 condition, the change in mass reaches a minimum around a

small neighbourhood of 31.0 % for all the heating rates, indicating complete reduction of wüstite into metallic iron. In contrast, carburization starts to dominate at 37–38 % under CO exposure conditions, leading to the formation of cementite and solid carbon deposition, in the form of graphite (Fig. 2d). From this stage onwards, the TGA curve begins to rise, showing a weight increase until it reaches a plateau. The curve, once it starts to rise, shows three sections with different slopes. In
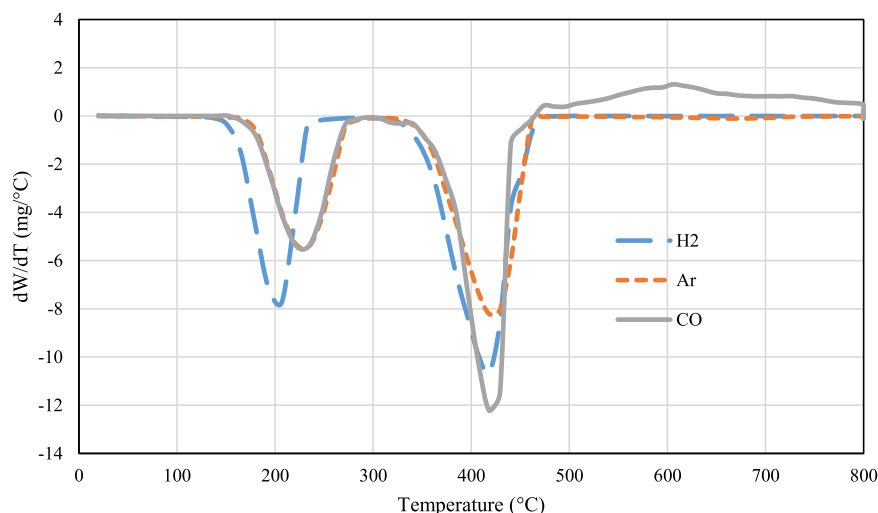
Fig. 4. First derivative with respect to time of the thermogravimetric curves, at a heating rate of 5 °C/min.

the first section, reduction (leading to weight loss), carburization and graphite formation (leading to weight gain) all occur simultaneously. Once the reduction of iron oxides is complete, carburization and graphite deposition persist, leading to a measurable increase in sample mass (Fig. 1c). After full carburization of the iron, the system enters a regime dominated solely by graphite deposition, causing the mass gain rate to decline. This process continues until the CO gas flow is terminated. Consequently, the sample mass increases steadily throughout the 5-minute isothermal hold at 800 °C (Fig. 1c), indicating ongoing reaction kinetics. Due to the simultaneous occurrence of these reactions, it is not possible to determine the final temperature of the range in which the reduction reaction takes place. For this reason, in Table 1, for the reduction step under CO, only the starting temperature of the reaction is indicated.

When the atmosphere is replaced with Ar during cooling, the mass stabilizes, reflecting cessation of reactive processes.

The DSC tests, at the heating rate of 5 °C/min, show the heat flow generated during the reactions, Fig. 3a–c. The generated power is negative, indicating the endothermic nature of the reactions. Specifically, the peaks are clearly visible in correspondence with the sections characterized by weight loss, which correspond to dehydration, decomposition, and reduction reactions. The trend of the DSC curves in the cases of H_2 and Ar is similar (Figs. 3a, 3b); the difference is that in a reducing atmosphere of H_2, the reduction reaction also occurs. The reduction reaction is known to be endothermic (23 kJ/mol Fe), which is why the second peak is higher in the case of H_2 atmosphere compared with Ar atmosphere.

For the sample treated in CO gas (Fig. 3c), there is a first peak of absorbed heat occurring simultaneously with water evaporation and a second peak due to the decomposition of the solid (reaction (2)). However, this peak is lower than the H_2 one (-33 %) since the reduction of wüstite with CO is exothermic (-17.9 kJ/mol Fe). Additionally, in the presence of iron, graphitic deposition takes place, which is also exothermic. For this reason, once the reverse Boudouard reaction dominates, the DSC curve shifts to a positive signal, exhibiting a peak that corresponds to the maximum rate of graphite deposition.

4. Discussion

As shown by the results in Table 1 and Fig. 1, the reaction steps occur at higher temperatures and shorter times as the heating rate increases. For example, in Ar, the dehydration step occurs in approximately 45 min at a heating rate of 2 °C/min, and in 11 min at 10 °C/min.

Additionally, the plateau duration shortens progressively with

increasing heating rate. At very high rates exceeding 50 °C/min, the plateau becomes negligible, causing reaction steps to overlap and preventing kinetic analysis. The maximum temperature (T_m) at which dehydration and decomposition occur also depends on the heating rate, and as the heating rate increases, it shifts towards higher temperatures.

In H_2 atmosphere, dehydration occurs at a slightly lower temperature (e.g., at 134°C at $\beta = 2$ °C/min, 9 % lower compared with that in Ar and CO atmospheres (at 147 °C at $\beta = 2$ °C/min)). The latter exhibits an almost identical profile in the dehydration phase. This difference in the onset temperature of dehydration in H_2 versus Ar and CO atmospheres, was also observed in the study by Carles et al. [25]. The authors attributed this phenomenon to the higher diffusivity of H_2, owing to its smaller molecular size, which facilitates penetration into interparticle pores. This enhanced gas-solid contact was suggested to promote more efficient heat transfer between the powder and the hot gas stream. Kawasaki et al. [29], studying the reduction of hematite pellets with H_2 and CO, estimated the gaseous diffusion rate constant (k_D), in g cm^{-1} min^{-1}, for both H_2 and CO. The results show that H_2 has significantly higher constants. For example, at 870°C, considering a pellet of 1.7–1.8 cm, the k_D for H_2 is 0.025, while for CO, it is 0.007 g cm^{-1} min^{-1}.

The solid decomposition step (reaction (2)) is evident for all three samples in different gas atmospheres: in the initial minutes following the activation of the reaction, whose activation time and temperature are reported in Table 1, the slope of the weight curve for the sample is similar (Fig. 4). It can therefore conclude that the decomposition step is influenced solely by heat, and that the gas used does not play a direct role in it [25].

As the reaction progresses, the slope for CO and H_2 increases (Fig. 4), while that for Ar decreases until the reaction is exhausted as it approaches complete decomposition to wüstite, as confirmed by XRD results (Fig. 2). The samples treated under an argon atmosphere are composed of wüstite, magnetite, and metallic iron, indicating that part of the wüstite has undergone disproportionation.

It is interesting to note how the curve initially stabilizes at a 41.2 % weight, before gradually approaching 39.7 %, which corresponds to the weight of wüstite (Fig. 1a). This phenomenon has also been observed by Hermanek et al. [24]. During the last part of the decomposition phase, some of the CO generated reacts with the solid to form iron carbide according to the following reaction:

$$3FeC_2O_4(s) + 2CO(g) \rightarrow Fe_3C(s) + 7CO_2(g) \tag{11}$$

This sluggish reaction is accompanied by weight loss. The small portion of cementite formed during this reaction then further slowly degrades at temperatures above 600 °C into iron and solid carbon,

Table 2
X-ray powder diffraction results.

Weight %				
β (°C/min)		2	5	10
Ar	Fe	10.2	12.0	12.2
	Fe$_3$O$_4$	26.3	18.4	19.2
	FeO	63.5	69.6	68.6
H$_2$	Fe	100.0	100.0	100.0
CO	C	54.4	48.3	36.8
	Fe$_3$C	45.8	51.7	63.2

according to reaction (12). This behaviour was reported by Hermanek et al. [24], who observed the progressive decomposition of iron carbide into α-iron through Mössbauer spectroscopy.

$$Fe_3C(s) \rightarrow 3Fe(s) + C(s) \qquad (12)$$

The wüstite disproportionates in varying amounts depending on the heating rate (Table 2). No presence of carbon is detected in the XRD results (Fig. 2b), which is likely due to its very small weight percentage (< 1.5 wt%).

The decomposition and reduction phases occurring under hydrogen and CO atmospheres result in steeper slopes of the weight curve. This phenomenon is even more evident in the case of CO, where the reduction occurs at a faster rate compared to H$_2$. This can be easily explained by analysing the reduction equilibria of wüstite with H$_2$ and CO (Fig. 5). Within the temperature range of interest, it can be seen that the thermodynamics of reduction with CO is more favourable than that with H$_2$, resulting in a higher reaction rate.

When the sample is subjected to reduction with CO, it is observed that, at all heating rates investigated, the curve starts to rise again at a weight percentage between 37 % and 38 %, due to carburization and graphite deposition. The activation of the Boudouard reaction and carburization, therefore, depend more on the composition of the solid rather than the temperature, as the carburization reaction depends on the presence of iron, which acts as a reactant, while graphite deposition reaction is catalysed by iron. For this reason, these two reactions are ignited when the decomposition is complete, and the reduction to metallic iron has begun. The results of the XRD analysis (Table 2) confirm that when using CO as reductant, the final solid is composed of cementite and graphite. At lower heating rates, as the residence time increases, the amount of graphite also increases.

To prevent excessive CO consumption in a reactor, it is important to determine the point of complete reduction. At this point, the process can be stopped by setting the correct solid residence time in the furnace. This prevents the onset of the Boudouard reaction, in which CO is converted into unwanted CO$_2$ and carbon.

Under H$_2$ exposure conditions. a complete reduction is achieved, and the XRD results confirm that the final solid is composed of 100 % metallic iron.

Carles et al. [25] performed the same TGA tests in Ar (Fig. 6a) and H$_2$ (Fig. 6b), the trend of the curves is identical. However, Carles' reactions [25] activate earlier, at slightly lower temperatures (15 %), and exhibit steeper slopes. The discrepancy is attributable to the different setups used. Specifically, Carles et al. [25] employed a sample with a mass up to ten times lower (viz., 0.02–0.04 g) and larger gas-solid ratios (viz., ~ 2 l min^{-1}g^{-1}).

The DSC results (Fig. 3) also confirm the findings obtained from the TGA experiments. In all cases, the first peak is attributed to the evaporation of water, the second to the decomposition of iron (II) oxalate into wüstite, and the third to its further reduction to metallic iron. After the reduction, in H$_2$, the absorbed power returns to almost zero, and then, as the temperature increases, the absorbed power grows linearly. This is due to phase transformations without weight changes. This trend is also visible in the results that had been published by Hermankova et al. [23] and Hermanek et al. [24].

Simultaneously with the decomposition reaction, the disproportionation of wüstite (reaction (3)) takes place also. This reaction does not involve any measurable mass change and is, therefore, not detectable through TGA analysis. However, it is a thermodynamically exothermic reaction, with a reaction enthalpy of – 15.17 kJ per mole of iron.

In a reducing atmosphere, the disproportionation process is difficult to quantify, as the wüstite formed by decomposition is simultaneously reduced to metallic iron. In contrast, under an inert atmosphere, wüstite disproportionates into iron and magnetite [31]. This behaviour is consistent with the results reported by Hermankova et al. [23]. This is particularly evident from the XRD pattern of the sample at the end of the thermal treatment under argon, where the presence of wüstite, metallic iron, and magnetite is clearly detected (Fig. 2b). The XRD analysis also shows that the amount of disproportionated wüstite decreases with increasing heating rate. This can be explained by the fact that the disproportionation reaction is faster than the synproportionation, where synproportionation is the reaction where Fe^0 and Fe^{3+} react to form Fe^{2+}.

Therefore, at lower heating rates, it is reasonable to conclude that a greater fraction of wüstite undergoes conversion below 570 °C.
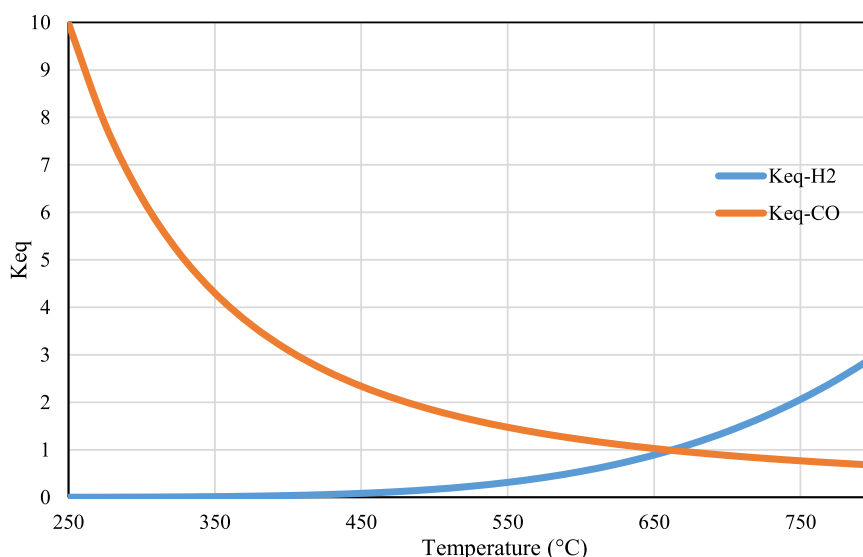
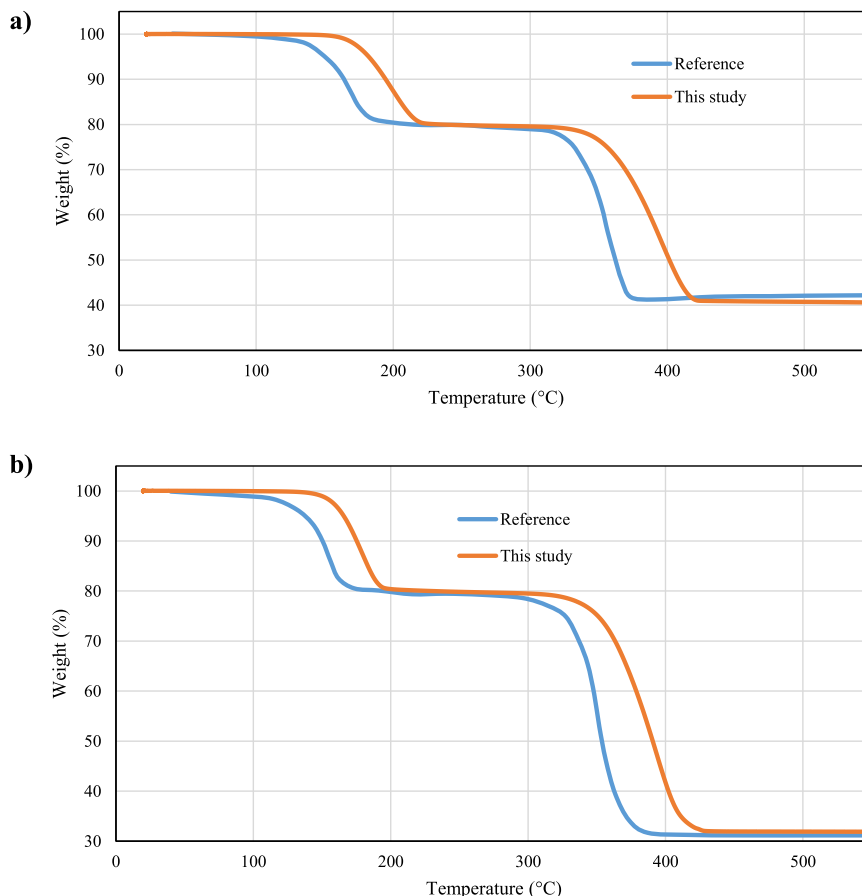**Fig. 5.** Wüstite reduction equilibrium [30].

a)

b)

Fig. 6. Comparison with literature curves [25]: 6a in Ar at 2 °C/min, 6b H$_2$ at 2 °C/min.

Likewise, lower heating rates also favour the reformation of wüstite via synproportionation, simply because the duration of the thermal treatment increases. However, since the disproportionation is the faster process, the net result is that the final amount of wüstite in the sample decreases as the heating rate increases.

The heat released by the disproportionation reaction contributes to reducing the intensity of the endothermic peak observed in the DSC curve under Ar, which corresponds to the decomposition step. This peak is noticeably lower compared to that observed in H$_2$ atmosphere (-30 %), while it is slightly higher than the one recorded in CO atmosphere (+ 4 %).

Once the temperature reaches a value around 570 °C (Fig. 3a), the reverse reaction occurs, namely the synproportionation of iron and magnetite to form wüstite, which is an endothermic process (15.17 kJ/mol Fe). In Fig. 3a, the DSC curve confirms this phenomenon, where a small endothermic peak is observed at 577 °C, followed by a linear decrease in the signal throughout the rest of the thermal treatment. This decreasing trend of the curve, which does not level off towards zero, indicates that the reaction rate of the synproportionation process is increasing over time and, more importantly, that the reaction is not yet complete. This suggests that not all the magnetite and metallic iron have been reconverted into wüstite by the end of the thermal treatment.

In the case of CO, the trend is different because exothermic reactions take place, namely the reduction of wüstite to iron and the Boudouard reaction, whereas the carburization of iron to iron carbide is slightly endothermic.
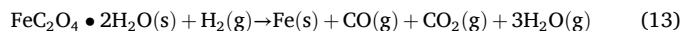
In this context, the global reduction reaction of iron oxalate salt with H$_2$ requires 253 kJ/mol Fe. Of this amount, 87 kJ/mol Fe is needed for the dehydration reactions, 142 kJ/mol Fe for the decomposition reaction, and finally, the reduction of wüstite requires 23 kJ/mol Fe (Aspen Plus library). Consequently, approximately 35 % of the total heat is absorbed by the dehydration process. This occurs because each mole of iron (II) oxalate contains 2 moles of water.
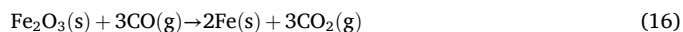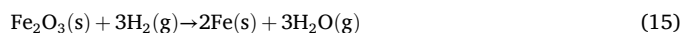
To reduce the amount of heat that needs to be supplied to the system, one possible solution is to introduce an anhydrous solid into the furnace. Comparing the reduction process of the iron salt with the direct reduction of hematite using H$_2$, which requires approximately 50 kJ/mol Fe (Aspen Plus library), it is evident that, from an energy perspective, the iron salt reduction process demands significantly more energy.

However, at the same time, as indicated by the reaction stoichiometry (13), the reduction of the salt requires only 1 mol of H$_2$ per mole of metallic iron produced, whereas the direct reduction process requires as much as 1.5 moles of H$_2$ per mole of iron (15). The same applies when CO is used as the reducing agent (14), (16). Furthermore, experimental apparatus has shown that the reactions initiate and proceed at relatively low temperatures, significantly lower than those required for the direct reduction process, which takes place in the range of 700–900°C.

Global iron (II) oxalate dihydrate reduction reaction:

$$FeC_2O_4 \bullet 2H_2O(s) + H_2(g) \rightarrow Fe(s) + CO(g) + CO_2(g) + 3H_2O(g) \qquad (13)$$

$$FeC_2O_4 \bullet 2H_2O(s) + CO(g) \rightarrow Fe(s) + CO(g) + 2CO_2(g) + 2H_2O(g) \qquad (14)$$
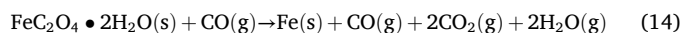
Global hematite reduction reaction (DRI process)

$$Fe_2O_3(s) + 3H_2(g) \rightarrow 2Fe(s) + 3H_2O(g) \qquad (15)$$

$$Fe_2O_3(s) + 3CO(g) \rightarrow 2Fe(s) + 3CO_2(g) \qquad (16)$$

It is crucial to reduce the energy consumption of the thermal treatment. Consequently, it is important to investigate the extraction of iron oxides in a non-aqueous environment. Gumtya et al. [32] tested the dissolution of oxalic acid in ethanol, thus providing an alternative to the use of water as a solvent. The results showed that the solubility of oxalic
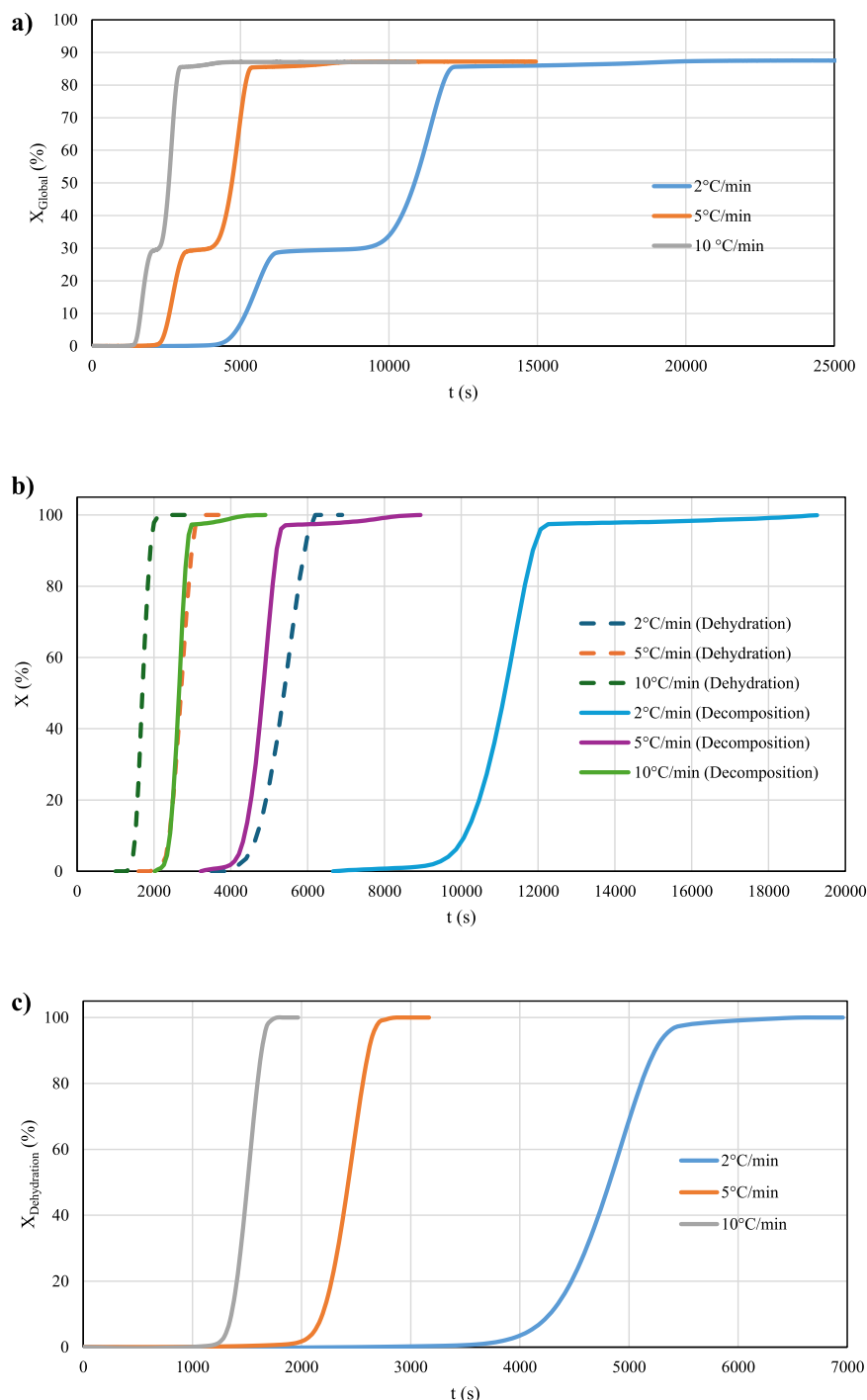
a)

T_m (Dehydration)$=593.55*\beta^{0.067}$
T_m (Decomposition)$=780.67*\beta^{0.046}$

b)

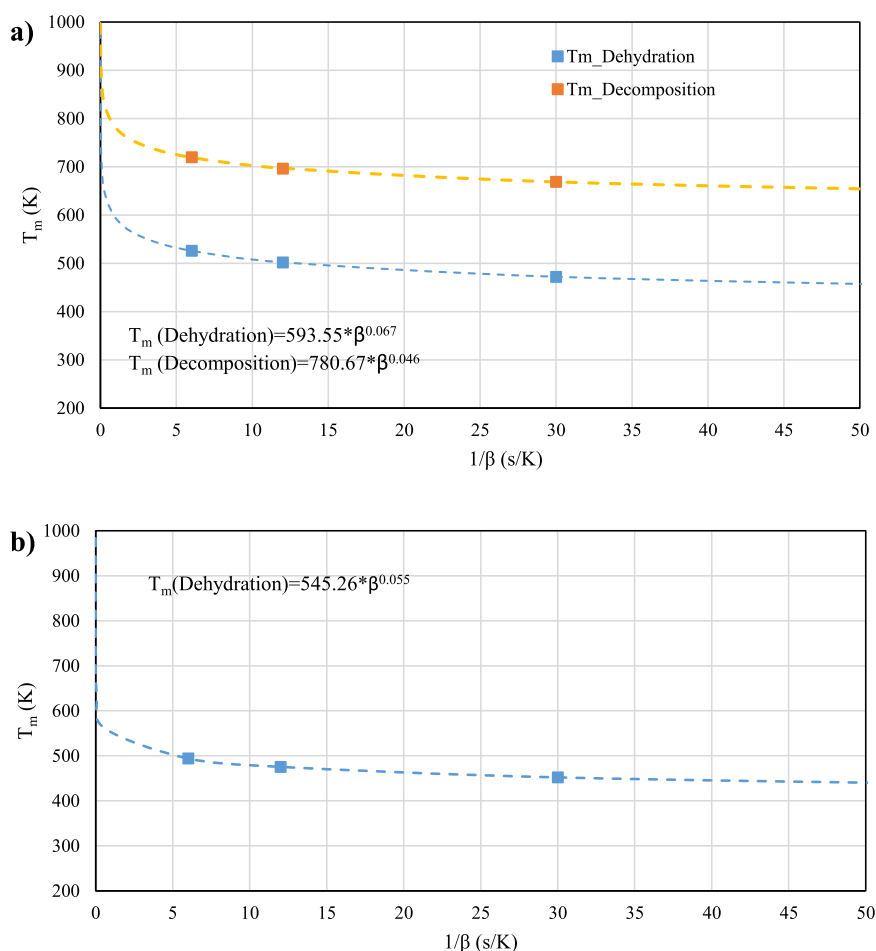T_m(Dehydration)$=545.26*\beta^{0.055}$

Fig. 8. T_m as a function of β in 8a Ar and 8b H_2. T_m: peak reaction temperature.

reused as a reducing agent, while providing a makeup to compensate for CO losses due to the Boudouard reaction. Thus, there is no need to resort to another reducing agent such as H_2.

Furthermore, the total heat required is obviously lower compared to the H_2 case, however, even in this case, it would be important to start the process with an anhydrous salt.

It is important to highlight the carbon footprint of the oxalate reduction process. During the decomposition step, one mole of CO and one mole of CO_2 are released. To subsequently reduce wüstite to metallic iron, either one mole of H_2 or one mole of CO is required, producing one mole of H_2O or CO_2, respectively. From these reactions, the carbon footprint of the reduction stage can be quantified, corresponding to 788 kg_{CO2}/t_{Fe} in the case of hydrogen and 1576 kg_{CO2}/t_{Fe} when CO is used. To this, the heat required to compensate for the endothermicity of the reduction step must be added. This can be achieved using electric heaters powered by renewable energy, as is already practiced in industrial applications [33].

Clearly, hydrogen represents a greener reducing agent compared to CO. However, Trinca et al. [22] proposed a process scheme in which the CO_2 generated is captured and recycled through the electrolytic regeneration of oxalic acid, the reagent needed for leaching iron oxides. This approach significantly mitigates the overall carbon footprint of the process.

4.1. Kinetic modelling

TGA analyses revealed that the evaporation step begins earlier in H_2 atmosphere compared to CO and Ar, which exhibit similar behavior. This is supported by the activation energy, which is lower for H_2 (58 kJ/

mol) than for CO and Ar (62 kJ/mol). The kinetics of thermal decomposition, however, are independent of the atmosphere. Therefore, the activation energy remains almost the same for all gases (90 kJ/mol). Carles et al. [25] identified the activation energy of the dehydration and decomposition reactions in H_2 as 85 and 152 kJ/mol. It should be noted, however, that Carles et al. results were obtained from a single curve with a heating rate of 5 °C/min, whereas the results of this study were derived from multiple curves with different heating rates.

A different consideration applies to the reduction steps in a reducing atmosphere. The reduction reaction begins before the decomposition is fully completed, causing the two steps to overlap. In the case of CO, carburization and graphite formation reactions must also be taken into account. Therefore, it is imprecise to establish reduction kinetics from non-isothermal TGA curves. Nevertheless, the reduction of wüstite with H_2 and CO is a well-known and extensively studied phenomenon in literature. Several studies report detailed kinetics, such as those conducted by Hou et al. [34] and Hou et al. [35]. This also holds true for the carburization and carbon deposition reactions by CO, whose kinetics have been reported by Knapp et al. [36], for example.

An alternative approach was adopted to determine the reaction kinetics, particularly for the two reactions whose kinetics are not reported in the literature: evaporation and decomposition. As already observed from the TGA results, and in the literature [25], the decomposition reaction is independent of the surrounding atmosphere. Therefore, the decomposition kinetics were determined from tests conducted in Ar. Such kinetics remain valid also for gas mixtures other than pure Ar. A different behaviour is observed for the dehydration reaction, which occurs more rapidly in H_2 compared to Ar and CO.

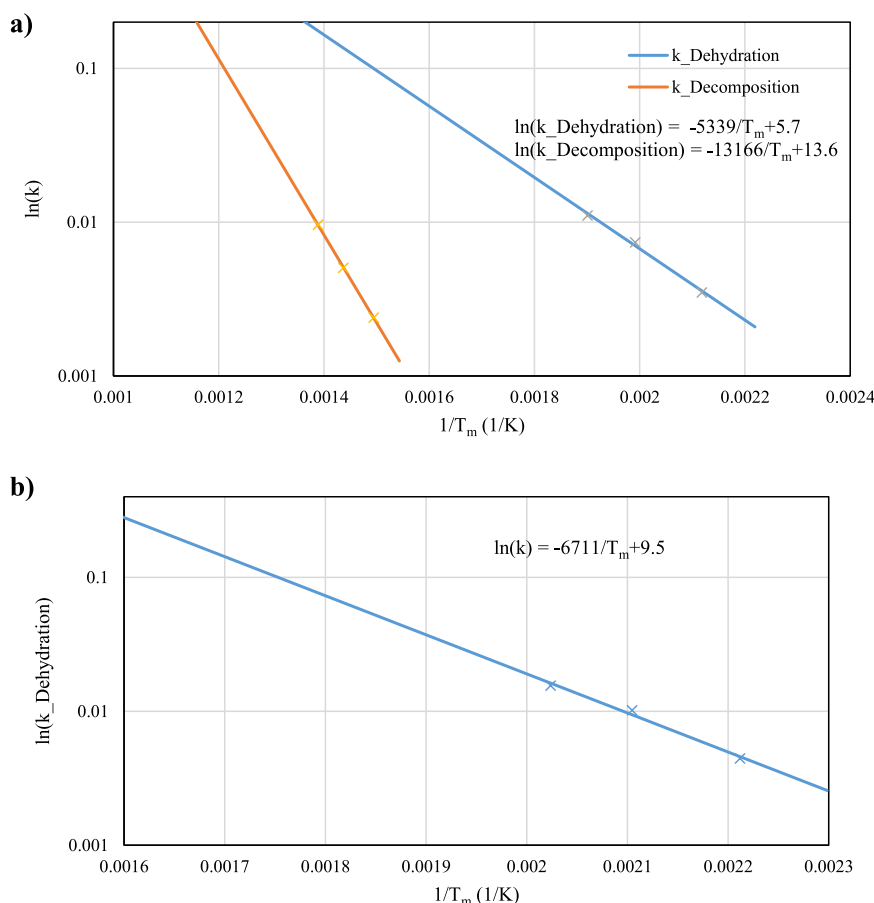Fig. 7a reports the conversion-time graph, derived from Eq. (15). It is

a)

b)

Fig. 9. k as function of $1/T_m$ in 9a Ar and 9b H_2. T_m: peak reaction temperature.

evident that the two reactions, as extensively discussed, occur in series, separated by a plateau region. As the heating rate increases, this plateau decreases until it disappears at high heating rates, indicating that the two reactions overlap. The presence of the plateau allows the two reaction steps to be analysed separately, as shown in conversion-time graph (Fig. 7b, c), derived from Eqs. (17) and (18). The global (17), dehydration (18) and decomposition conversion (19) are expressed as:

$$X_{Global}(\%) = \frac{W_L}{W_{FeC_2O_4 \bullet 2H_2O} - W_{Fe}} * 100 \tag{17}$$

$$X_{Dehydration}(\%) = \frac{W_L - W_{FeC_2O_4 \bullet 2H_2O}}{W_{FeC_2O_4 \bullet 2H_2O} - W_{FeC_2O_4}} * 100 \tag{18}$$

$$X_{Decomposition}(\%) = \frac{W_L - W_{FeC_2O_4}}{W_{FeC_2O_4} - W_{FeO}} * 100 \tag{19}$$

where W_L represents the weight loss (mg), $W_{FeC_2O_4 \bullet 2H_2O}$, $W_{FeC_2O_4}$, W_{FeO}, W_{Fe} represent the weight (mg) of the initial sample, the sample after complete dehydration, the sample after complete decomposition to wüstite, and the sample after complete reduction to metallic iron.

The conversion (%), as documented in Fig. 7, exhibits a sigmoidal trend and can be expressed with the following zero-order relationship (20):

$$X(\%) = 100/(1 + e^{(-k(t-t_0))}) \tag{20}$$

Thus, the conversion depends on time and the kinetic constant k. t_0 is a time that depends on the activation time (t_{act}) of the reactions.

The experimental data (Fig. 7) were plotted and fitted using the sigmoidal Eq. (20). Three kinetic constants were extracted for each reaction (three for evaporation and three for decomposition). The kinetic

constant follows an Arrhenius trend and can be expressed as (21):

$$k = k_0 e^{(-\frac{E_a}{RT_m})} \tag{21}$$

where T_m is the peak reaction temperature. As shown in Fig. 8, the peak temperature T_m is closely related to the heating rate β: as β increases, T_m also increases (Table 1).

This implies that the kinetic constant k depends on β. The kinetic constants were plotted as a function of $1/T_m$, from which k_0 and E_a were determined (Fig. 9).

Additionally, t_{act} varies with β, as shown in Fig. 10. There is a linear relationship between t_0 and t_{act}:

$$t_{0Dehydration}(Ar) = 1.262 * t_{actDehydration}(Ar) \tag{22}$$

$$t_{0Dehydration}(H_2) = 1.430 * t_{actDehydration}(H_2) \tag{23}$$

$$t_{0Decomposition} = 1.618 * t_{actDecomposition} \tag{24}$$

Finally, the overall kinetics can be expressed as X (t, β) and graphed in Fig. 11. The trend is clear: as β increases, the activation times shift toward zero, and the slope of the curve increases until it reaches an infinite slope for β approaching infinity. The mathematical model proves to be consistent, as it fits the experimental results obtained from the TGA curves with accuracy.

Moreover, it also reliably predicts the plateau between dehydration and decomposition, as shown by the overlap between the end time of the dehydration reaction and the onset time of the decomposition reaction. This behaviour remains valid even at heating rates significantly above those tested, confirming the robustness of the model even when applying it beyond the regime probed by experiments (β = 2, 5, 10 °C/

a)

$t_{act}\_Dehydration = 415.62*\beta^{-0.68}$

$t_{act}\_Decomposition = 523.70*\beta^{-0.74}$
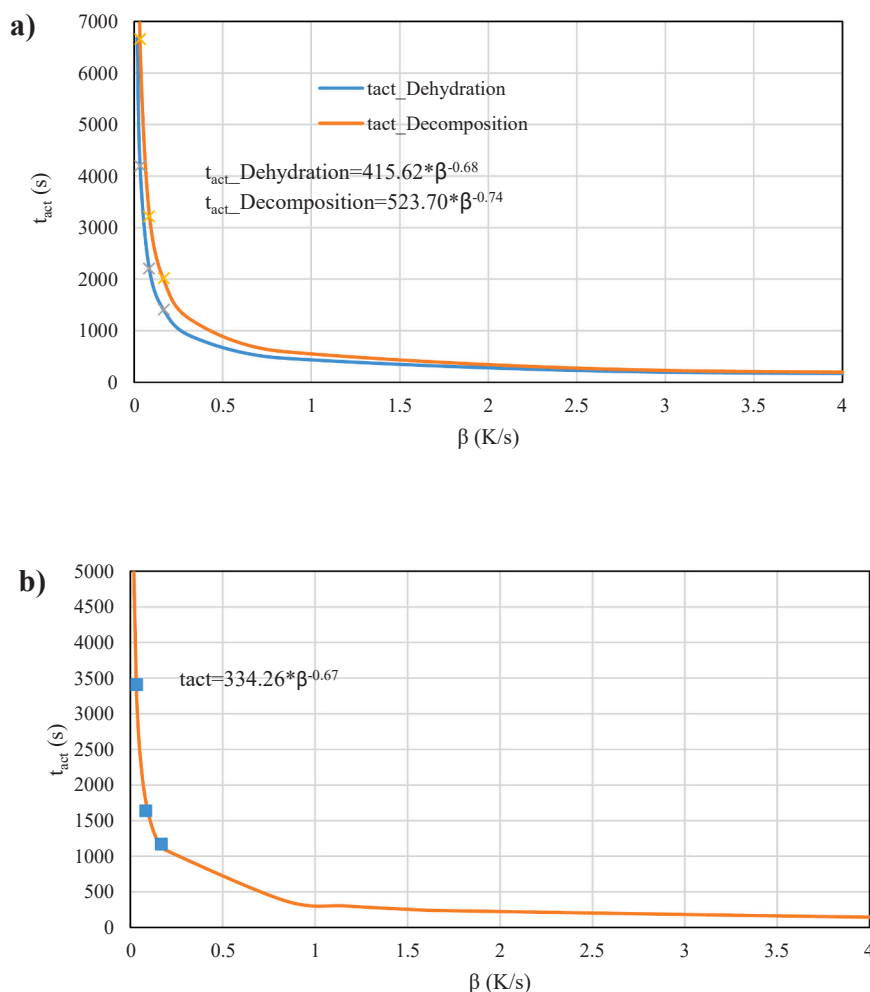
b)

$tact = 334.26*\beta^{-0.67}$

Fig. 10. t_{act} in function of beta in 10a Ar and 10b H$_2$. t_{act}: activation time of the reactions.

min).

These kinetics is important because, for a fixed β, it allows understanding how the conversion of decomposition and dehydration reactions evolves over time. Therefore, it is possible to design a reduction reactor based on the reactor type, where different reducing gases can also be used. Moreover, the model remains valid even at heating rates typical of industrial reactors (β ~ 100 °C/min), which are significantly higher than those used in this study and in all other works reported in the literature (β ≤ 10 °C/min). Future studies should apply this kinetics to conduct a techno-economic assessment of the entire steel production process from low-grade ores through a hydro-pyrometallurgical route.

5. Conclusions

The study investigated the decomposition and reduction behaviour of iron (II) oxalate under non-isothermal conditions with linear heating rates of 2, 5, and 10 °C/min using thermogravimetry analysis (TGA), differential scanning calorimetry (DSC), and X-ray diffraction (XRD). The main conclusions are summarized as follows:

- The reaction process of iron (II) oxalate involves sequential dehydration, decomposition, and reduction steps. In H$_2$, faster kinetics are observed due to enhanced thermal exchange by fast hydrogen diffusion. In Ar atmosphere, the final product is wüstite, which partially disproportionates into magnetite and iron during final cooling at temperatures below 570 ℃. Full reduction to metallic iron occurs in H$_2$ and CO, while CO leads to carburization, forming

cementite and depositing graphitic carbon via the Boudouard reaction, both catalyzed by metallic porous iron.
- DSC results revealed that reactions in Ar and H$_2$ are endothermic. Dehydration proved to be an energy-intensive step. Achieving anhydrous precursors is therefore crucial for energy-efficient processing. Kinetic analysis via the Kissinger method yielded activation energies of 58 kJ/mol (H$_2$), 62 kJ/mol (CO and Ar) for dehydration, and 90 kJ/mol for decomposition, independent of gas atmosphere. A kinetic model was developed to describe the dehydration and decomposition reactions as a function of heating rate, enabling future process simulations of the steel production process from low-grade ore.
- The study advances kinetic modelling of the evaporation and thermal decomposition steps of FeC$_2$O$_4$·2H$_2$O in inert and reducing atmospheres and supports the development of innovative hydro-pyrometallurgical processes for low-grade iron ores. This process offers advantages such as moderate operational temperatures (< 500 °C) and reduced gas consumption compared with hydrogen-based direct reduction of iron oxides, with potential for CO recycling and reuse, which is generated during decomposition of FeC$_2$O$_4$·2H$_2$O.

CRediT authorship contribution statement

Antonio Trinca: Writing – original draft, Validation, Methodology, Investigation, Data curation, Conceptualization. **Isnaldi R Souza Filho:** Writing – review & editing, Supervision, Data curation. **Yan Ma:** Writing – review & editing, Supervision, Methodology. **Özge Özgün:** Data
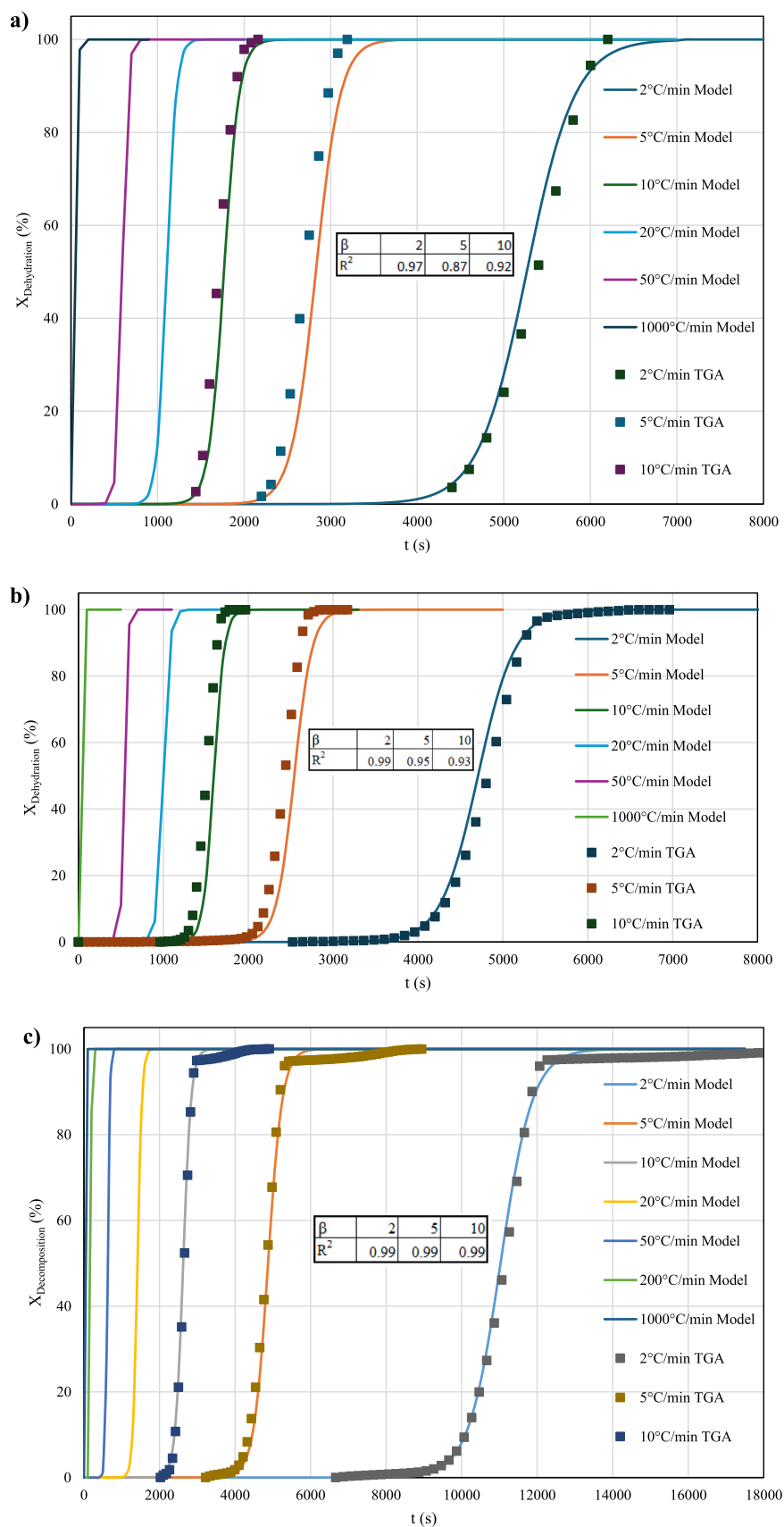
Fig. 11. Model of the conversion as a function of beta and time of the dehydration in 11a Ar and 11b H$_2$ and 11c decomposition.

Data availability

Data will be made available on request.

References

[1] M.L.T. Triviño, R.Q. Raguindin, Sustainable practices for carbon neutrality: catalytic applications of steel slag waste for carbon dioxide mitigation, J. Environ. Chem. Eng. 13 (3) (2025) 116995, https://doi.org/10.1016/J.JECE.2025.116995.

[2] IEA, Steel and aluminium, Paris, 2023. Accessed 27 August 2025. [Online]. Available: ⟨https://www.iea.org/reports/steel-and-aluminium⟩.

[3] Green Transformation needs clear orientation – forecasting the steel demand in 2030 – Bronk & Company. Accessed 10 April 2025. [Online]. Available: ⟨https://bronk-company.com/en/2023/01/forecast-steel-demand-2030/⟩.

[4] D. Raabe, et al., Circular steel for fast decarbonization: thermodynamics, kinetics, and microstructure behind upcycling scrap into high-performance sheet steel, Annu. Rev. Mater. Res. 54 (1) (2024) 247–297, https://doi.org/10.1146/ANNUREV-MATSCI-080222-123648/CITE/REFWORKS.

[5] Y. Ma, et al., Hierarchical nature of hydrogen-based direct reduction of iron oxides, Scr. Mater. 213 (2022) 114571, https://doi.org/10.1016/J.SCRIPTAMAT.2022.114571.

[6] D. Raabe, The materials science behind sustainable metals and alloys, Chem. Rev. 123 (5) (2023) 2436–2608, https://doi.org/10.1021/ACS.CHEMREV.2C00799/ASSET/IMAGES/LARGE/CR2C00799_0047.JPEG.

[7] F. Patisson, O. Mirgaux, Hydrogen ironmaking: how it works, Metals 10 (7) (2020) 922, https://doi.org/10.3390/MET10070922.

[8] V. Vogl, M. Åhman, L.J. Nilsson, Assessment of hydrogen direct reduction for fossil-free steelmaking, J. Clean. Prod. 203 (2018) 736–745, https://doi.org/10.1016/J.JCLEPRO.2018.08.279.

[9] D. Spreitzer, J. Schenk, Reduction of iron oxides with hydrogen—a review, Steel Res. Int. 90 (10) (2019) 1900108, https://doi.org/10.1002/SRIN.201900108.

[10] R. Niu, et al., Hydrogen-enhanced deformation in pearlite, Acta Mater. 281 (2024) 120327, https://doi.org/10.1016/J.ACTAMAT.2024.120327.

[11] M.M.A. Aslam, et al., Technologies for recovery of iron from red mud: processes, challenges and opportunities, Sustain. Mater. Technol. 41 (2024) e01053, https://doi.org/10.1016/J.SUSMAT.2024.E01053.

[12] S. Cheng, et al., Advances in the integrated recovery of valuable components from titanium-bearing blast furnace slag: a review, Sustain. Mater. Technol. 44 (2025) e01384, https://doi.org/10.1016/J.SUSMAT.2025.E01384.

[13] A. Cam, M. Deniz Turan, M. Deniz Turan, Iron removal from bauxite by oxalic acid and further Al extraction by high-pressure alkali leaching, J. Sustain. Metall., vol. 9, pp. 710–22, 1234, ⟨https://doi.org/10.1007/s40831-023-00680-7⟩.

[14] P. Vehmaanperä, T. Sihvonen, R. Salmimies, A. Häkkinen, Dissolution of magnetite and hematite in mixtures of oxalic and nitric acid: mechanisms and kinetics, Minerals 12 (5) (2022), https://doi.org/10.3390/min12050560.

[15] S.O. Lee, T. Tran, B.H. Jung, S.J. Kim, M.J. Kim, Dissolution of iron oxide using oxalic acid, Hydrometallurgy 87 (3–4) (2007) 91–99, https://doi.org/10.1016/J.HYDROMET.2007.02.005.

[16] P. Santawaja, S. Kudo, A. Tahara, S. Asano, J.I. Hayashi, Dissolution of iron oxides highly loaded in oxalic acid aqueous solution for a potential application in iron-making, ISIJ Int. 62 (12) (2022) 2466–2475, https://doi.org/10.2355/isijinternational.ISIJINT-2020-726.

[17] P. Santawaja, S. Kudo, A. Mori, A. Tahara, S. Asano, J.I. Hayashi, Sustainable iron-making using oxalic acid: the concept, a brief review of key reactions, and an experimental demonstration of the iron-making process, ACS Sustain. Chem. Eng. 8 (35) (2020) 13292–13301, https://doi.org/10.1021/acssuschemeng.0c03593.

[18] Y. Dong, J. Chen, C. Li, H. Zhu, Decoloration of three azo dyes in water by photocatalysis of fe (III)-oxalate complexes/H2O2 in the presence of inorganic salts, Dyes Pigments 73 (2) (2007) 261–268, https://doi.org/10.1016/j.dyepig.2005.12.007.

[19] A. William, L. Dudeney, I.I. Tarasova, Photochemical decomposition of trisoxalatoiron(III): a hydrometallurgical application of daylight, Hydrometallurgy 47 (1998) 243–257.

[20] H. Tanvar, B. Mishra, Hydrometallurgical recycling of red mud to produce materials for industrial applications: alkali separation, iron leaching and extraction, Metall. Mater. Trans. B: Process Metall. Mater. Process. Sci. 52 (5) (2021) 3543–3557, https://doi.org/10.1007/s11663-021-02285-5.

[21] H. Hickling, Preparation and Properties of Iron Powders Produced by Reduction of Ferrous Oxalate Dihydrate, Loughborough University of Technology Library, 2018 ([Online]. Available: ⟨https://hdl.handle.net/2134/34948⟩).

[22] A. Trinca, G. Vilardi, N. Verdone, Hybrid hydro-pyrometallurgy route for green steel: design and cost analysis of innovative and negative carbon dioxide emissions industrial-scale plants with different iron ore grades, Energy Convers. Manag. 332 (2025) 119776, https://doi.org/10.1016/J.ENCONMAN.2025.119776.

[23] P. Hermankova, M. Hermanek, R. Zboril, Thermal decomposition of ferric oxalate tetrahydrate in oxidative and inert atmospheres: the role of ferrous oxalate as an intermediate, Eur. J. Inorg. Chem. (7) (2010) 1110–1118, https://doi.org/10.1002/ejic.200900835.

[24] M. Hermanek, R. Zboril, M. Mashlan, L. MacHala, O. Schneeweiss, Thermal behaviour of iron(II) oxalate dihydrate in the atmosphere of its conversion gases, J. Mater. Chem. 16 (13) (2006) 1273–1280, https://doi.org/10.1039/b514565a.

[25] V.Â. Carles, P. Alphonse, P. Tailhades, A. Rousset, Study of thermal decomposition of FeC2O4-2H2O under hydrogen, Thermochim. Acta 334 (1999) 107–113.

[26] H. Ogasawara, N. Koga, Kinetic modeling for thermal dehydration of ferrous oxalate dihydrate polymorphs: a combined model for induction period– surface reaction–phase boundary reaction, Phys. Chem. A (2014), https://doi.org/10.1021/jp500619q.

[27] Q. Fradet, M. Kurnatowska, U. Riedel, Thermochemical Reduction of Iron Oxide Powders with Hydrogen: Review of Selected Thermal Analysis Studies, Elsevier B. V., 2023, https://doi.org/10.1016/j.tca.2023.179552.

[28] H.E. Kissinger, Reaction Kinetics in Differential Thermal Analysis, 1956. [Online]. Available: ⟨https://pubs.acs.org/sharingguidelines⟩.

[29] E. Kawasaki, J. Sanscrainte, T.J. Walsh, Kinetics of reduction of iron oxide with carbon monoxide and hydrogen, AlChE J. (1962).

[30] M.S. Valipour, Mathematical modeling of a non-catalytic gas-solid reaction: hematite pellet reduction with syngas, Trans. C: Chem. Chem. Eng. 16 (2) (2009).

[31] W.K. Jozwiak, E. Kaczmarek, T.P. Maniecki, W. Ignaczak, W. Maniukiewicz, Reduction behavior of iron oxides in hydrogen and carbon monoxide atmospheres, Appl. Catal. A Gen. 326 (1) (2007) 17–27, https://doi.org/10.1016/J.APCATA.2007.03.021.

[32] S.K. Gumtya, S.C. Lahiri, S. Aditya, Studies on the Solubility and Dissociation Constants of Oxalic Acid in Aquo + Ethanolic Mixtures and Determination of Single-ion Gibbs Energy of Transfer from Aqueous to Aquo + Ethanolic Mixtures, Oldenbourg Wissenschaftsverlag, 2002.

[33] A. Trinca, G. Vilardi, N. Verdone, Towards carbon neutrality: the ammonia approach to green steel, Energy Convers. Manag 326 (2025) 119482, https://doi.org/10.1016/J.ENCONMAN.2025.119482.

[34] B. Hou, B. Zhang, H. Li, Q. Zhu, Study on kinetics of iron oxide reduction by hydrogen, Chin. J. Chem. Eng. 20 (1) (2012) 10–17, https://doi.org/10.1016/S1004-9541(12)60357-7.

[35] B. Hou, H. Zhang, H. Li, Q. Zhu, Determination of the intrinsic kinetics of iron oxide reduced by carbon monoxide in an isothermal differential micro-packed bed, Chin. J. Chem. Eng. 23 (6) (2015) 974–980, https://doi.org/10.1016/j.cjche.2015.01.006.

[36] M.R. Knapp, K. Li, W.O. Philbrook, Kinetics carbon of reactions between magnetite and monoxide between 723 and 823 K, Metall. Trans. B (1974).